



Wide-field sensorless adaptive optics swept-source optical coherence tomographic angiography in rodents

XIANG WEI,^{1,2} TRISTAN T. HORMEL,¹ SHAOHUA PI,¹ BINGJIE WANG,¹ JOHN C. MORRISON,¹ AND YALI JIA^{1,2,*}

¹Casey Eye Institute, Oregon Health and Science University, 515 SW Campus Dr., Portland, Oregon, 97239, USA

²Department of Biomedical Engineering, Oregon Health and Science University, 3303 SW Bond Avenue, Portland, Oregon, 97239, USA

*Corresponding author: Jiaya@ohsu.edu

Received 4 August 2022; revised 3 September 2022; accepted 4 September 2022; posted 6 September 2022; published 23 September 2022

In this study, we present a sensorless adaptive optics swept-source optical coherence tomographic angiography (sAO-SS-OCTA) imaging system for mice. Real-time graphics processing unit (GPU)-based OCTA image acquisition and processing software were applied to guide wavefront correction using a deformable mirror based on signal strength index (SSI) from both OCT and OCTA images. High-resolution OCTA images with aberrations corrected and contrast enhanced were successfully acquired. Fifty-degree field of view high-resolution montaged OCTA images were also acquired. © 2022 Optica Publishing Group

<https://doi.org/10.1364/OL.472387>

Optical coherence tomography (OCT) is a three-dimensional imaging method [1] that has been broadly applied to biological tissues. With micrometer resolution and fast imaging speed, this technique has many applications in clinical ophthalmology and ocular research [2–5]. Optical coherence tomographic angiography (OCTA) is a non-invasive, dye-free OCT image processing technique that can be used to image retinal capillaries and choroidal vasculature *in vivo* [6–11]. It is based on extracting blood flow information by computing motion contrast between multiple repeated scans from identical scan locations. Compared with conventional two-dimensional fluorescein angiography, OCTA is high resolution, can provide volumetric information, and does not require an exogenous contrast agent that might carry the risk of anaphylaxis [12].

Coupled with murine models, OCTA has been used to investigate normal ocular circulation and disease pathophysiology [13]. However, aberrations introduced by imperfections in a mouse's lens can significantly reduce the OCTA image quality [14,15]. To solve this problem, wavefront correction is commonly used. Adaptive optics (AO) is a wavefront correction technique that has been used for human and non-human primate retinal imaging [16,17]. It has two major components: a wavefront sensor used to measure the wavefront error, and a deformable mirror that can be shaped on the fly to correct it. However, accurate measurement of aberrations with a wavefront sensor is quite challenging in small eyes because

strongly scattering anatomic layers, such as the retinal pigmented epithelium, choroid, and nerve fiber layer, have the potential to confound measurements. In addition, the integration of a wavefront sensor and deformable mirror complicates the OCT system design.

To overcome this drawback, Jian *et al.* introduced sensorless AO (sAO) OCT systems [18–24]. Instead of using a wavefront sensor to provide feedback, the sAO system uses real-time structural OCT images sharpness to indicate the wavefront correction progress [25]. The introduction of sAO has significantly simplified AO systems, and at the same time, increased reliability [18]. The development of GPU-based, real-time OCT/OCTA processing has also significantly increased the sAO optimization efficiency [26]. In this study, we present an sAO-OCTA system with a real-time OCT/OCTA-based image optimization process that has been designed for rodents. In this approach, novel OCT and OCTA quality metrics are synergistically integrated to help guide the sAO optimization.

The system in this study uses a 100-kHz swept-source laser (Axsun, Excelitas Technologies Corp.). The laser has a center wavelength of 1060 nm with a 100-nm sweep range. The maximum axial resolution is 5 μm in the air. Two 50/50 split ratio fiber optic couplers (Thorlabs Inc.) are used to build the Mach-Zehnder interferometer (MZI) (Fig. 1). The reference arm uses a custom-designed motorized optical delay line. A piezoelectric deformable mirror (Thorlabs Inc.) with 15-mm pupil, 40-actuator array, and high-stroke (defocus ± 17.6 μm, astigmatism ± 18.4 μm, coma ± 6.8 μm) is included in the sample arm to correct wavefront errors, and a 5-mm galvanometer scanner (Scanner Max) is also integrated. The sample arm telescope has a magnification of 6.7, the beam size on the pupil is 0.6 mm, and the spot size on the retina is 3 μm for mice. A balanced detector with a 400-MHz bandwidth (Thorlabs Inc) is used to collect the interference pattern. An ATS-9373 digitizer (Alazar Technologies Inc.) is used to convert the analog signal into a digital signal. A GPU-based real-time OCT/OCTA data acquisition algorithm [26] running on a Nvidia RTX 2060 GPU acquires the raw spectrum data and provides image quality feedback to adjust the deformable mirror. We use a conventional OCT system design with an improved sAO sample arm design. Instead of

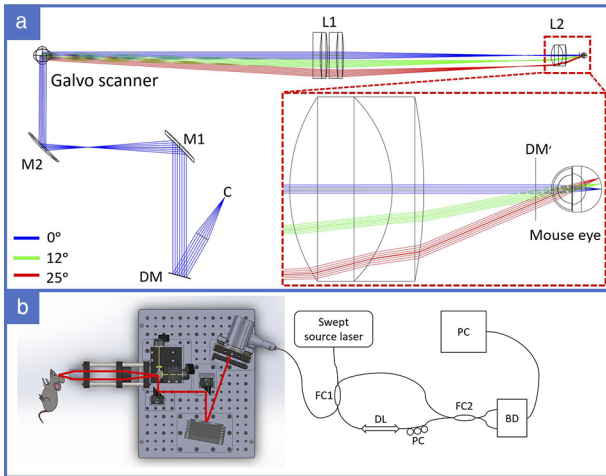


Fig. 1. Sample arm optical design and system configuration. (a) Performance of the sAO sample arm design simulated using OpticStudio (Zemax, LLC). The sample arm contains a fiber optic collimator (C) with a beam size of 8 mm. The light from the collimator is reflected by the deformable mirror (DM) at an incident angle of 15°. Ninety-degree off-axis parabolic reflectors ($M_1, f = 50.8$ mm; $M_2, f = 25.4$ mm) reduce the beam size to 4 mm. A set of galvanometer scanners scan the laser beam at different angles. The scanning lens contains two achromatic doublets with effective focal length of 100 mm (L1). The ocular lens is a single achromatic doublet with 15 mm focal length (L2). The conjugated DM image (DM') is designed to be placed 1 mm in front of the cornea. (b) Sample arm mechanical design is based on the OpticStudio (Zemax, LLC) simulation results. The optical mounts are 3D printed to minimize calibration difficulty. The system contains a 100-kHz swept source laser. Laser light emitted from the swept-source laser is split into a sample arm and reference arm using a 50/50 split ratio fiber optic coupler (FC1). In the reference arm, a motorized optical delay line (DL) is applied. In the sample arm, the beam size is 0.6 mm. The backscattered light from the sample arm interferes with the reference light in the fiber optic coupler (FC2) with a split ratio of 50/50. A balanced detector (BD) is used to digitize the optical signal and transfer it to the PC.

using a lens to reduce the beam size, here, we are using a pair of off-axis parabolic reflectors to reduce the beam size. The optical design of the sample arm has been verified using a Zemax mouse eye model (OpticStudio, Zemax, LLC) to accurately simulate the aberration of the laser beam with different incident angles.

Aberration analysis was performed using a model mouse eye that is modified according to a previous publication [14]. Three different beams with three different incident angles were studied (Fig. 2). Incident angles corresponded to a small field of view (0°), medium field of view (12°), and large field of view (25°). At 0°, no significant aberrations could be found in the Zernike coefficients or the spot diagram. However, when the incident angle was increased to 12°, multiple aberrations (defocus, astigmatism, coma) could be observed in the Zernike coefficients as well as the spot diagram. When the incident angle was further increased to 25°, more aberrations could be found (defocus, astigmatism, coma, trefoil); these are apparent in both the Zernike coefficient and the spot diagram. Since mixed aberrations were introduced at large scanning angles, only optimizing the focus was no longer sufficient for high quality imaging in this

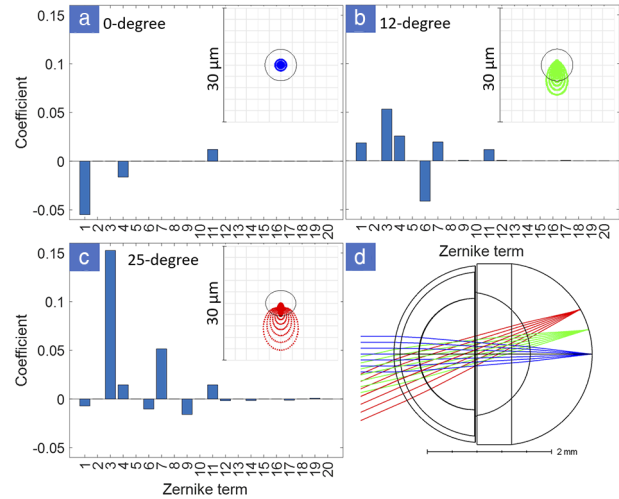


Fig. 2. Aberration simulation results for different scanning angles. The first twenty Zernike coefficients are shown, with the spot diagram inset. Airy disk size is 3 μm. (a) At 0° incidence, few aberrations can be found in the spot diagram or the Zernike coefficients. (b) At 12° incidence, multiple different aberrations are apparent in the coefficient plot (Z3, Z4, Z6, Z7, and Z11). (c) At 25° incidence, more aberrations are apparent (Z3, Z4, Z6, Z7, Z8, and Z11). (d) Model mouse eye showing light paths from the three different incident angles (blue, 0°; green, 12°; red, 25°).

setting. To reduce the aberrations, a deformable mirror (DM) was added in the sample arm to modify the beam profile in real-time. An optimization process and algorithm were developed to control the DM. This optimization was based on the real-time calculation of the OCT signal strength index and the OCTA signal strength index. Due to the limitation of imaging speed, during the optimization, instead of using the *en face* image generated from a volumetric scan, here we are using a cross scan pattern containing a set of vertical and horizontal scans at the same position. The optimization is based on the vertical and horizontal scans. The OCT structural signal strength index (SSSI) was calculated using the mean of the structural OCT B-scan intensity in the target anatomic layer (inner retina in this study), and the OCTA signal strength index (ASSI) was calculated using the mean of the OCTA B-scan intensity in the same layer. In the beginning of each imaging session, due to the low image quality, there is not enough OCTA signal that can be used to evaluate the image quality, and hence the SSSI from the OCT structural image is used for initial adjustment. Once the image quality is improved and there is enough OCTA signal, the ASSI from the OCTA images is used for fine adjustments. The major contributors to image quality loss are low order aberrations like defocus, astigmatism, coma, and trefoil. The optimization process follows the order of these aberrations (Z1–Z16). For each optimization, the anatomic layer of interest in the mouse retina is selected. Both SSIs are calculated for each optimization step. The aberrations are then compensated according to the maximum of the signal strength indices [27]. The coarse adjustment based on the SSSI is applied first, followed by fine adjustment based on the ASSI.

During imaging, C57BL/6 mice were first anesthetized with 5% isoflurane for 5 minutes in a sealed chamber and then transferred to the imaging platform. The animal body temperature was maintained at 38.5°C using a water-warming blanket.

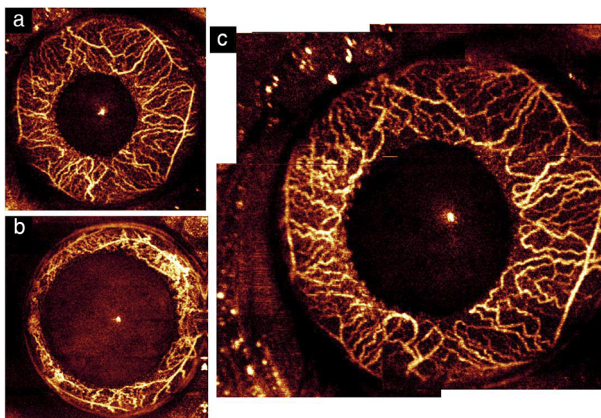


Fig. 3. OCTA images acquired from the mouse iris. The high image quality indicates the system aberrations have been largely removed. (a) Iris OCTA image acquired before full dilation, (b) iris OCTA image acquired after full dilation, (c) montaged high-resolution iris OCTA image captured prior to full dilation.

Oxygen with 3.5% isoflurane at a flow rate of 1 L/min was used to maintain the anesthesia status. A 1% tropicamide ophthalmic solution was used to dilate the pupil before imaging. Hypromellose (0.3%) lubricant eye gel was applied to moisten the cornea. All experimental procedures complied with the Association for Research in Vision and Ophthalmology statement for the use of animals in ophthalmic and vision research and were approved by the Institutional Animal Care and Use Committee (IACUC) of Oregon Health and Science University.

The OCT and OCTA images were processed using our previously developed GPU-based real-time OCT/OCTA image acquisition and processing software [26]. OCT data processing followed the standard swept source OCT data processing algorithm [28]. The raw interference fringe data were acquired linearly in k-space using a sampling clock generated from a built-in MZI. Digital dispersion compensation was used to compensate for the dispersion mismatch introduced by the sample arm lenses and the mouse eye. For each position, three repeated scans were acquired. The OCT image was generated using phase-stabilized complex decorrelation angiography (PSCD) [11].

Due to the application of parabolic reflector, the system aberration can be significant from misalignments. For each imaging session, the system aberrations were carefully calibrated and optimized by imaging a resolution testing target (1951 USAF). The defocusing and reference arm were also changed to a preset position for iris imaging. A raster scan pattern with 450×450 line scans (with three repetitions) was applied, with OCT and OCTA images generated in real time. *En face* OCTA images from the iris were first acquired and generated using mean projection across the whole imaging depth without sAO optimization (Fig. 3). OCTA images from before dilation [Fig. 3(a)] and after dilation [Fig. 3(b)] were acquired. A high-resolution montaged iris OCTA image was also developed before full dilation [Fig. 3(c)]. These images were acquired without applying the sAO optimization to verify there is no significant system aberrations; with sAO, it is possible to further improve the image quality. After imaging the iris, retinal OCT/OCTA images were also acquired. A 25° field of view was achieved with the pupil fully dilated. The OCT *en face* images were generated using mean projection across the whole

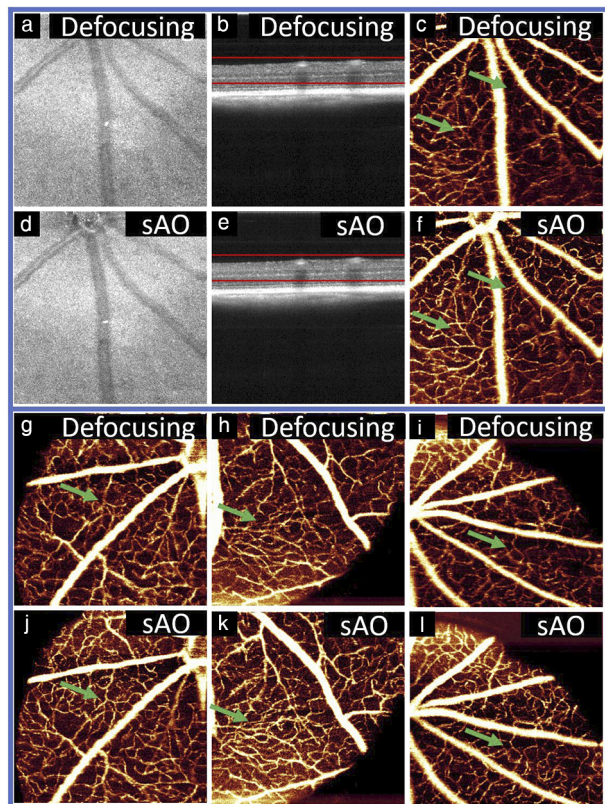


Fig. 4. OCT/OCTA images before and after sAO optimization. Images before optimization: (a) OCT *en face*; (b) OCT B-scan; (c) OCTA *en face*. Images after optimization: (d) OCT *en face*; (e) OCT B-scan; (f) OCTA *en face*. Red lines in panels (b, e) indicate the region over which projections were performed. The OCTA image in panel (f) is noticeably enhanced by the sAO technique. (g-i) OCTA *en face* images in different retinal regions defocusing sAO optimization only, (j-l) OCTA *en face* images in different retinal regions with sAO optimization. Arrows indicate improvement in the sAO images.

imaging depth, while the OCTA *en face* images were generated using the maximum projection method [29]. For images without high order sAO optimization, only defocusing was optimized. For images with high order sAO optimization, astigmatism, coma, and trefoil were also optimized (in addition to defocus). The total correction time is within 30 seconds. Both images with defocusing and high order sAO optimization had reasonably high structural OCT image quality [Figs. 4(a), 4(b), 4(d), 4(e)]. However, OCTA images with high order sAO optimization [Figs. 4(f), 4(j), 4(k), 4(l)] had noticeably higher image quality than images with only defocusing optimization [Figs. 4(c), 4(g), 4(h), 4(i)].

Fifty-degree wide-field single volume OCT and OCTA images could also be acquired by this system in either a single shot or with montage (Fig. 5). The single shot scanning pattern also used 450×450 line scans with three repeats. With this approach, aberrations could not be consistently corrected across the entire 50° image since their type and strength vary with incident angle. In addition, due to the limited image sampling density, capillaries could not be completely resolved [Fig. 5(c)]. However, a montaged OCTA image, formed by combining four 25° field of view volume scans acquired at different positions,

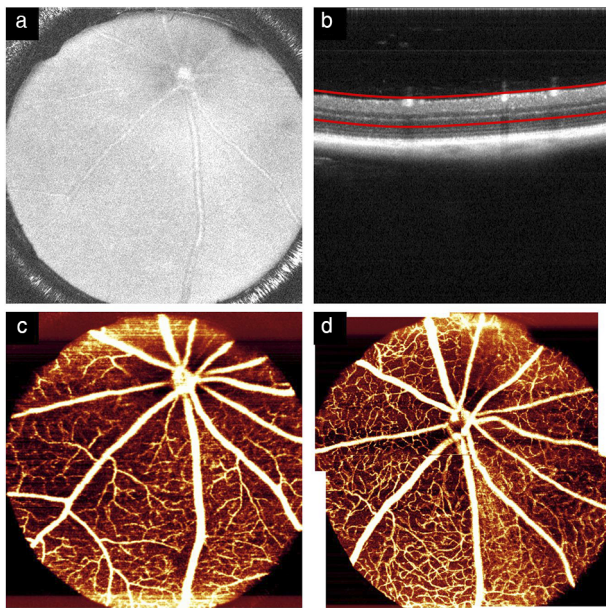


Fig. 5. Single volume 50° wide-field (a) OCT *en face*, (b) OCT B-scan, and (c) inner retinal OCTA. The red lines indicate the region over which projections were performed. OCTA image quality is low due to the aberrations at large scanning angles and the insufficient sampling density. (d) 50° montaged wide-field sAO OCTA image.

resulted in a significantly improved image quality and better capillary resolution.

A wide-field sAO swept-source OCTA system with real-time OCT/OCTA data acquisition has been successfully developed. An OCT/OCTA SSI-based image optimization process was successfully applied to an sAO system, allowing OCTA images from both the iris and retina, with significant improvement in image quality. To the best of our knowledge, for the first time, a 50° high-resolution wide-field sAO OCTA retinal image was also successfully acquired by montaging four OCTA images. The novel implementation of both SSSI and ASSI in the sAO optimization process also provides an effective way to evaluate image quality and aberrations. By improving the OCTA image quality of mouse retinal and iris blood vessels, this sAO technique will enhance research and our understanding of retinal vascular diseases.

Funding. BrightFocus Foundation (G2020168); Research to Prevent Blindness (unrestricted departmental funding grant); National Institutes of Health (P30 EY010572, R01 EY010145, R01 EY024544, R01 EY027833, R01 EY031394, T32 EY023211).

Disclosures. Oregon Health and Science University (OHSU) and Yali Jia have a significant financial interest in Optovue, Inc. These potential conflicts of interest have been reviewed and managed by OHSU.

Data availability. Data underlying the results presented in this paper are not publicly available at this time but may be obtained from the authors upon reasonable request.

REFERENCES

- D. Huang, E. A. Swanson, C. P. Lin, J. S. Schuman, W. G. Stinson, W. Chang, M. R. Hee, T. Flotte, K. Gregory, C. A. Puliafito, and J. G. Fujimoto, *Science* **254**, 1178 (1991).
- M. R. Hee, J. A. Izatt, E. A. Swanson, D. Huang, J. S. Schuman, C. P. Lin, C. A. Puliafito, and J. G. Fujimoto, *Arch. Ophthalmol.* **113**, 325 (1995).
- A. F. Fercher, *J. Biomed. Opt.* **1**, 157 (1996).
- A. F. Fercher, W. Drexler, C. K. Hitzenberger, and T. Lasser, *Rep. Prog. Phys.* **66**, 239 (2003).
- W. Drexler and J. G. Fujimoto, *Optical coherence tomography: technology and applications*: Springer; 2015.
- S. Makita, Y. Hong, M. Yamanari, T. Yatagai, and Y. Yasuno, *Opt. Express* **14**, 7821 (2006).
- R. K. Wang, S. L. Jacques, Z. Ma, S. Hurst, S. R. Hanson, and A. Gruber, *Opt. Express* **15**, 4083 (2007).
- M. S. Mahmud, D. W. Cadotte, B. Vuong, C. Sun, T. W. Luk, A. Mariampillai, and V. X. D. Yang, *J. Biomed. Opt.* **18**, 050901 (2013).
- Y. Jia, O. Tan, J. Tokayer, B. Potsaid, Y. Wang, J. J. Liu, M. F. Kraus, H. Subhash, J. G. Fujimoto, J. Horngger, and D. Huang, *Opt. Express* **20**, 4710 (2012).
- D. Y. Kim, J. Fingler, R. J. Zawadzki, S. S. Park, L. S. Morse, D. M. Schwartz, S. E. Fraser, and J. S. Werner, *Proc. Natl. Acad. Sci. U. S. A.* **110**, 14354 (2013).
- X. Wei, T. T. Hormel, and Y. Jia, *Biomed. Opt. Express* **12**, 2419 (2021).
- L. A. Yannuzzi, K. T. Rohrer, L. J. Tindel, R. S. Sobel, M. A. Costanza, W. Shields, and E. Zang, *Ophthalmology* **93**, 611 (1986).
- S. Pi, A. Camino, X. Wei, J. Simonett, W. Cepurna, D. Huang, J. C. Morrison, and Y. Jia, *Biomed. Opt. Express* **9**, 5851 (2018).
- Y. Geng, L. A. Schery, R. Sharma, A. Dubra, K. Ahmad, R. T. Libby, and D. R. Williams, *Biomed. Opt. Express* **2**, 717 (2011).
- X. Liu, C.-H. Wang, C. Dai, A. Camesa, H. F. Zhang, and S. Jiao, *Curr. Eye Res.* **38**, 1235 (2013).
- R. J. Zawadzki, S. M. Jones, S. S. Olivier, M. Zhao, B. A. Bower, J. A. Izatt, S. Choi, S. Laut, and J. S. Werner, *Opt. Express* **13**, 8532 (2005).
- R. S. Jonnal, O. P. Kocaoglu, R. J. Zawadzki, Z. Liu, D. T. Miller, and J. S. Werner, *Invest. Ophthalmol. Visual Sci.* **57**, OCT51 (2016).
- Y. Jian, R. J. Zawadzki, and M. V. Sarunic, *J. Biomed. Opt.* **18**, 056007 (2013).
- Y. Jian, J. Xu, M. A. Gradowski, S. Bonora, R. J. Zawadzki, and M. V. Sarunic, *Biomed. Opt. Express* **5**, 547 (2014).
- K. S. Wong, Y. Jian, M. Cua, S. Bonora, R. J. Zawadzki, and M. V. Sarunic, *Biomed. Opt. Express* **6**, 580 (2015).
- D. J. Wahl, Y. Jian, S. Bonora, R. J. Zawadzki, and M. V. Sarunic, *Biomed. Opt. Express* **7**, 1 (2016).
- H. R. Verstraete, M. Heisler, M. J. Ju, D. Wahl, L. Bliek, J. Kalkman, S. Bonora, Y. Jian, M. Verhaegen, and M. V. Sarunic, *Biomed. Opt. Express* **8**, 2261 (2017).
- M. J. Ju, M. Heisler, D. Wahl, Y. Jian, and M. V. Sarunic, *J. Biomed. Opt.* **22**, 1 (2017).
- D. J. Wahl, R. Ng, M. J. Ju, Y. Jian, and M. V. Sarunic, *Biomed. Opt. Express* **10**, 252 (2019).
- M. Cua, D. J. Wahl, Y. Zhao, S. Lee, S. Bonora, R. J. Zawadzki, Y. Jian, and M. V. Sarunic, *Sci. Rep.* **6**, 32223 (2016).
- X. Wei, A. Camino, S. Pi, T. T. Hormel, W. Cepurna, D. Huang, J. C. Morrison, and Y. Jia, *Opt. Lett.* **44**, 1431 (2019).
- A. Camino, R. Ng, J. Huang, Y. Guo, S. Ni, Y. Jia, D. Huang, and Y. Jian, *Opt. Lett.* **45**, 2612 (2020).
- A. F. Fercher, C. K. Hitzenberger, M. Sticker, R. Zawadzki, B. Karamata, and T. Lasser, *Opt. Express* **9**, 610 (2001).
- T. T. Hormel, J. Wang, S. T. Bailey, T. S. Hwang, D. Huang, and Y. Jia, *Biomed. Opt. Express* **9**, 6412 (2018).